Guidance, Navigation and Control for Autonomous Cooperative Docking of CubeSats

Camille Pirat [(1)], Pierre-Alain Mäusli [(2)], Roger Walker [(3)], Finn Ankersen [(4)], Volker Gass[(5)]

[(1)] EPFL-Swiss Space Center, station 13, 1015 Lausanne, Switzerland, camille.pirat@epfl.ch
[(2)] EPFL, station 15, 1015 Lausanne, Switzerland, pierre-alain.mausli@epfl.ch
[(3)] ESA-ESTEC, Keplerlaan 1, 2201AZ Noordwijk, Netherlands, roger.walker@esa.int
[(4)] ESA-ESTEC, Keplerlaan 1, 2201AZ Noordwijk, Netherlands, finn.ankersen@esa.int
[(5)] EPFL-Swiss Space Center, station 13, 1015 Lausanne, Switzerland, volker.gass@epfl.ch

ABSTRACT

Is it possible to dock CubeSats in Low Earth Orbit? The challenges are mainly associated with the level of miniaturisation. A docking mechanism was designed, built and tested in the laboratory. Results show that a relative precision better than 1 cm and 2 degrees is required for the docking. The docking mechanism and metrology system, composed of a monocular camera and sets of light-emitting diodes, are contained within 0.5U volume and can thus be used on nano-satellites. The chaser and target satellites have a complete 3-axis attitude pointing capability and are equipped with available CubeSats attitude sensors and actuators. The chaser is further equipped with a 6 degrees of freedom low-thrust cold gas propulsion system. Different robust control schemes have been investigated and their stability and performance assessed. Non-linear Monte Carlo simulations have been performed to assess the Guidance, Navigation and Control (GNC) performance and fuel consumption. Results show that the proposed GNC is robust to the various sources of uncertainties and that a lateral accuracy better than 5 mm is obtained at docking. Furthermore, it is not affected by the loss of the star trackers or by illumination conditions and can thus take place on a variety of orbits.

1 INTRODUCTION

Is it possible to dock CubeSats in Low Earth Orbit? This question was not yet answered and is an open research subject. Today the best results have been obtained within the International Space Station (ISS) with the MIT SPHERES experiment [1], although the dynamic is not exactly representative of Low Earth Orbit (LEO). The aim of this research is to investigate the feasibility of an In-Orbit Demonstration (IOD) mission using two CubeSats, to demonstrate GNC algorithms and Rendezvous and Docking (RVD) technologies. Close proximity operations IOD missions have already been investigated within the European Space Agency (ESA) General Support Technology Programme (GSTP). It has shown that standard CubeSats actuators and sensors such as reaction wheels, star trackers, Global Navigation Satellite System (GNSS), and propulsion system have sufficient accuracy for achieving proximity operations such as fly-around or spin synchronisation [2]. To achieve CubeSats' RVD, three questions need to be answered. First, what is the required accuracy to dock two CubeSats, and with which docking mechanism? Secondly, what type of metrology system can provide the necessary accuracy and how robust can it be? Finally, what kind of controller can be used in combination with the metrology system which would guarantee a successful docking, coping with the large amount of uncertainties, and sensors and actuators noise? Several docking mechanisms for nano- and micro-satellites have been investigated. In [3], an androgynous mechanism is proposed and can manage 5 deg and 1.5 cm misalignment. It has however never been tested in space. To the authors knowledge, the only nano-satellite docking mechanism which has successfully been tested in space is the SPHERES Universal Docking Port (UDP) [4], which can tolerate up to 2 deg and 1 cm misalignment. To achieve such level of accuracy, the navigation should be approximately ten times

better. It has been demonstrated on-orbit that Carrier Phase Differential GPS (CDGPS) can achieve few centimetres relative accuracy [5]. Although such navigation solution can be used for the previous phases of a RVD mission, this level of accuracy is not sufficient for the docking itself. Furthermore, Line of Sight (LoS) constraints and possible multipath effects prevent the use of this sensor for the docking. Today, only two vehicles are performing autonomous RVD: the Russian Progress and Soyuz spacecraft. Their navigation is based on a radiofrequency solution, called Kurs, which requires several antennas and pointing mechanisms [6]. ESA own retired Automated Transfer Vehicle (ATV), which docked successfully with the ISS five times, was the first spacecraft ever to dock autonomously using a Vision-Based Navigation (VBN) solution [7]. An active monitoring of the docking was performed by the crew on-board the ISS, using a television camera and a cross-shaped pattern fixed on the ATV [8]. Vision-based techniques are also used for the autonomous docking of the MIT SPHERES [9]. ATV's heritage, camera miniaturisation capabilities, and potential for high accuracy navigation makes VBN very appealing. It may seem that the SPHERES UDP and VBN could be used as such for CubeSat RVD. However, the distances and illumination conditions involved for RVD are very different than within the ISS. Furthermore, SPHERES solution requires heavy image processing. A dedicated VBN system has thus been investigated which would allow for obtaining the complete relative state form 10 m range, and be robust to illumination conditions and stray light. However, having two separated volumes, for the docking mechanism and the VBN, is not optimal. It has thus been decided to design a docking mechanism which would include the VBN system and hold in ½ CubeSat Unit (U).

Several Multi-Input Multi-Output (MIMO) control schemes could be used to achieve the necessary docking accuracy. Three controllers are traded-off in this study: LQR, H_∞, and μ-synthesis and are of increasing complexity. Eventually, the VBN and selected controllers can be combined in a non-linear simulator, which includes all relevant sources of error and their performance regarding docking accuracy and fuel consumption can be evaluated. To drive the design of the GNC and docking mechanism, the following requirements are used: The docking mechanism shall be able to cope with misalignment up to 2 deg and 1 cm (3σ). The GNC shall have an accuracy of 1 deg and 5 mm at docking (3σ). Including a 100% margin in the control accuracy requirements allows to gain confidence in the overall GNC and docking system design.

This paper is structured as follow: in section 2, the mission scenario, different reference frames, and CubeSat configuration will be described. In section 3, the GNC will be described and will focus on the attitude determination and control system, VBN, and controller robustness. The docking mechanism will be presented in section 4. Finally, the results of the non-linear simulation are provided in section 5.

2 MISSION DESIGN & CUBESAT CONFIGURATION (2 pages)

Six reference frames are required to describe the problem and are shown in Figure 1:

1. The Earth Centred Inertial (ECI) frame has its origin at the centre of the earth and uses the J2000 definition.
2. The orbital frame or LVLH frame is centred on the satellite Centre of Mass (CoM) and is defined such that $\hat{z} = -\frac{\boldsymbol{r}}{r}$, where $\boldsymbol{r}$ is the satellite inertial position and is called R-bar. $\hat{y} = -\frac{\boldsymbol{r}\times\boldsymbol{v}}{|\boldsymbol{r}\times\boldsymbol{v}|}$, where $\boldsymbol{v}$ is the satellite velocity and is called H-bar. Finally, $\hat{x}$ completes the direct frame and is called V-bar.
3. The geometrical frame is fixed on the satellite structure and can be arbitrarily defined.
4. The body frame is located at the CoM of the satellite and has its axis aligned with the geometrical frame.
5. The docking frame is defined with respect to the geometrical frame and has its origin at the centre of the docking mechanism.

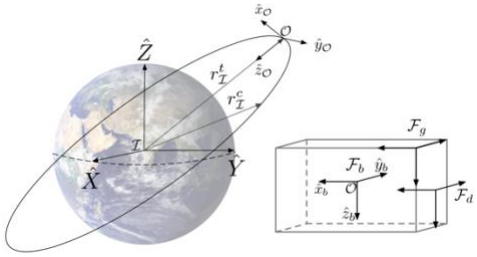

Figure 1: Reference frames.

Note that the body frame is not fixed to the geometrical frame as the CoM will vary throughout the mission.

2.1 Mission Scenario

The mission scenario under consideration is depicted in Figure 2.

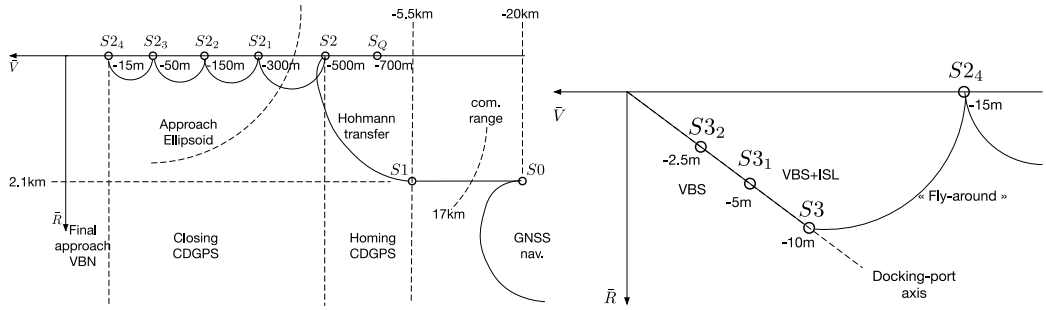

Figure 2: General RVD scenario (left) and close-range scenario (right).

The point S0, called first aim point, corresponds to the end of the phasing. Based on safety margins, thrust, navigation and propagation errors, it was decided to place S0 20 km behind and 2.1 km below the target. Assuming that the CDGPS filter needs 15 min to converge and taking 15 min margins to prepare for the manoeuvre from S1 to S2, the Inter Satellite Link (ISL) shall have a communication range of at least 17 km, as it is required for the relative navigation. The Hohmann transfer shall start 5.5 km behind the target and will bring the satellite at point S2, 500 m behind the target, outside the approach ellipsoid. The approach ellipsoid is centred on the target and has dimension 400 m along V-bar and 200m along R-bar. From this point the closing can begin and will bring the chaser to point $S2_4$ by successive radial manoeuvres which ensure passive safety. At point $S2_4$, the target attitude and docking port orientation is communicated to the chaser satellite using the ISL and the final approach starts. A two-burn fly-around manoeuvre will align the chaser with the target docking port axis at point S3 and the VBN will be initiated. At this point the target attitude will be required by the VBN and thus the ISL will still be active. The chaser will perform a forced translation to point $S3_1$. At this point, the VBN will be switched to a higher precision mode which does not require the ISL and will be used to move the chaser to point $S3_2$. A safety Station Keeping (SK) will be performed at 2.5 m range to ensure that the GNC is working nominally and allows for systems check. Eventually the last translation will start and will drive the chaser towards the target docking port. All the translations are performed with a speed of 1 cm/s. The placement of the different hold points has been determined based on the burn duration it would take to initiate the radial manoeuvres. In [2], 3.3 minutes burn have been used and it has been realised that the amount of uncertainties it was inducing led to a requirement violation if not combined with a high bandwidth controller. It has thus been decided to keep all the open-loop ΔV burn duration below 3 min. For the closing (until $S2_4$), the open-loop ΔV is 0.26 m/s. The closed-loop control will increase this value and a total ΔV estimate will be provided in section 5. During fly-around and translations, the error along each axis shall be smaller than 5% of the range (3σ) and the attitude error smaller than 4 deg around each axis (3σ).

2.2 CubeSats Configuration

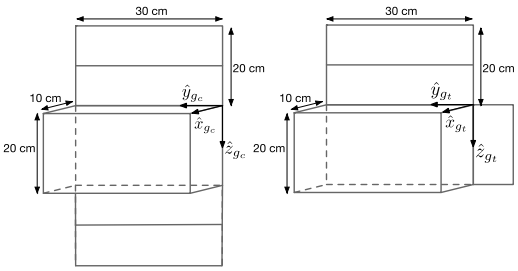

Figure 3: Chaser (left) and target (right) CubeSats dimensions and geometrical frame.

To accommodate the various sensors, actuators and avionics, the 6U form factor has been selected. The chaser and target dimensions are depicted in Figure 3. No precise power simulations were performed yet and it is possible that no deployable solar array will be needed. However, the ones shown in Figure 3 have been dimensioned and positioned such as to increase differential drag and disturbances. The non-symmetry of the target will contribute to degrading the attitude pointing and is interesting to have to assess the GNC capabilities. The docking ports location, with respect to the CoM, are [10, 10, 10] cm for the chaser and [-10, 10, 10] cm for the target. The chaser port frame is aligned with the geometrical frame and the target port is rotated in the geometrical frame by 50 deg around each axis using the 1-2-3 Euler sequence. It places the two docking ports outside the 6U envelop. Although this is not realistic, this configuration represents the worst-case position one could expect for CubeSats and will increase the coupling between the position and rotations. This target docking port orientation places the point S3 at [-4.3, -8.6, -2.7] m in the LVLH frame. Both CubeSats have a complete Attitude, Determination and Control System (ADCS). The chaser is further equipped with a 6 DoF propulsion system. The sensors and actuators are described in section 3. The chaser has a dry mass of 10 kg and can carry up to 2 kg of fuel. The target mass is 11 kg.

3 GNC DESCRIPTION

3.1 Attitude, Determination and Control System

Both CubeSats have the same ADCS. The target will use it for the complete duration of the mission whereas the chaser will switch to a dedicated navigation system for the docking phase. The sensor suite for both CubeSats include a magnetometer, a star tracker, a gyroscope, sun sensors and a GNSS receiver. The GNSS receiver is required by the ADCS for the on-board magnetic field and sun position model prediction. The GNSS receiver is simply modelled by a white noise with a standard deviation of 2 m (3σ) [10]. The AMR magnetometer from ZARM [11] is modelled with a white noise of 1μT (1 % error on a range of ±100 μT) and a misalignment of 1 deg. The on-board magnetic field model is degraded by the GNNS error and a low-correlation noise is added, amounting 1% (2σ) of the current field value [12]. The sun sensors have a field of view (FoV) of 60 deg and are modelled by considering a steady state error of 0.5 deg when the sun is vertical to the sensor. As the angle with respect to the sensor local vertical increases, the error increases quadratically until reaching 2.5 deg. As for the magnetic field, the on-board sun model is degraded by the GNSS measurement. The sun sensor and magnetometer models are both based on the assumption that a proper calibration will be performed prior to the flight and on-orbit if necessary. The star tracker model is based on [13] and white noises of 200 arc seconds around the roll axis and 30 arc seconds around the pitch and yaw axis are used. Baffle options are available but their capabilities not precisely known, an exclusion angle of 45 deg from boresight is thus assumed. Finally, the gyroscope is based on the STIM 300 [14]. As in the case of sensor loss the ADCS can only rely on its gyroscope, some efforts have been invested in the development of an accurate model. Apart from usual scale factor, misalignment, non-orthogonality and quantisation, three different sources of noise are used. The angular random walk

(ARM) is a simple white noise. The rate random walk (RRW) (bias instability) is modelled as a brown noise which has a $1/f^2$ power spectrum density (PSD). Finally, a flicker noise (pink noise) is added and has a 1/f PSD [15], [16]. In the model, the following values are used: 0.15 deg/$h^{1/2}$ for the ARW, 3 deg/h/ $h^{1/2}$ for the RRW and 0.5 deg/h for the flicker noise. The Allan variance of the model and of the STIM 300 are compared in Figure 4. Although the gyroscope model has a higher noise density at low frequency, corresponding to the ARW, and will consequently be more conservative, the model obtained is very satisfying.

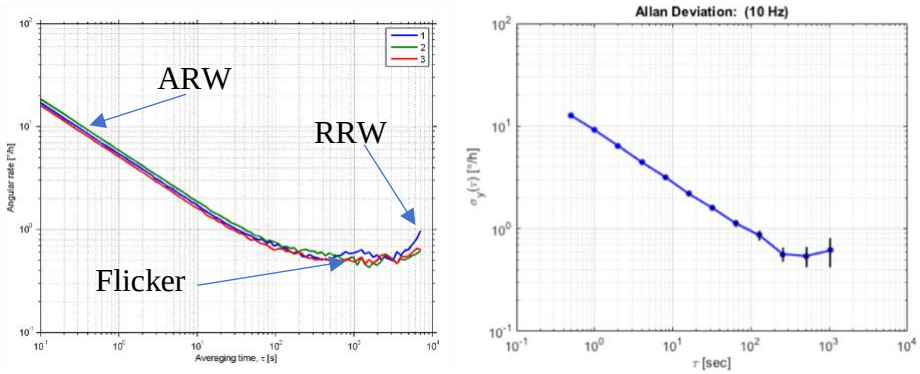

Figure 4: STIM 300 Allan variance (left) and gyros model variance (right).

The two satellites are equipped with three reaction wheels (RW). The RW model can be simplified considering only three sources of error: white noise, low-correlation time noise, and cage instabilities. The white noise has a standard deviation of 10^{-5} Nm (3σ). This value has been scaled based on the Rosetta flight results [17]. The low-correlation noise has a correlation time of ½ sample and a standard deviation of $2 \cdot 10^{-5}$ Nm (3σ). These two noises are coherent with the specifications of the various CubeSats RW available [18], [19], which suggest an accuracy better than 5 round per minute (RPM) which corresponds to a torque noise of ~$3 \cdot 10^{-5}$ Nm. Although friction and viscous effects should also be considered and can be simply modelled, the lack of data about CubeSats RWs made this task impossible. Finally, a cage instability perturbation is added. It is modelled as steps having an amplitude of 10% of the maximum torque capability [20]. These steps occur several times per day and last for a few minutes. This is the effect of the bearing cage switching between stable vibration modes. The ADCS (and more generally the GNC) is sampled at 1 Hz and RW are operated at 1500 RPM. Thus, high frequency noises are aliased in the low-correlation time noise and this RW model should be representative enough. To prevent the RW reaching higher speed or saturating, a simple proportional control law using magnetic rods is used [21]. The magnetic rods have a maximum dipole capability of 0.4 Am^2 [22]. The output of the reaction wheel compared to a command torque is provided in Figure 5.

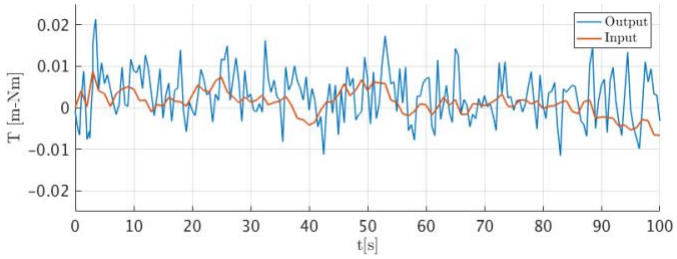

Figure 5: Reaction Wheel model output.

Note that operating the RW at a fixed speed allows for a better internal dipole characterisation which will improve the magnetometer measurements. The Extended Kalman Filter (EKF) for the attitude determination is purely kinematic and thus does not suffer from inertia or torques input uncertainties [23]. Apart from the attitude itself, the gyroscope bias is part of the state vector, and is thus estimated

and accounted for in real time. The bias model only considers ARW and RRW. Each sensor is included in the filter and dynamically enabled/disabled depending on availability. Finally, the control is performed using a quaternion feedback regulator [24]

3.2 Navigation

CDGPS is used to navigate the chaser from the first aim point S0 (Figure 2) until it is aligned with the target docking port, at a range of 10 m (point S3). It is simulated using a white noise with a standard deviation of 10 cm (3σ). From 10 m range a more accurate navigation is required to obtain the relative position and attitude between the docking ports (Port to Port (P2P) navigation). The P2P attitude and position dynamics describing the motion between the two docking ports has a strong coupling. Indeed, a rotation of the target attitude will change its docking port attitude and position, and the chaser will consequently need to account for it in its navigation and control scheme. During the development of the VBN, it has been realised that in order to be attractive, the docking mechanism and the metrology system should hold in a 1U surface. This way, it could be accommodated on a variety of CubeSats. The VBN and coupled dynamic used for the control and navigation are thoroughly described in [25]. The navigation solution will be briefly recalled here. To accommodate the docking mechanism and the VBN system in a compact package, only one simple camera can be used leading to a fixed focal length. Thus, accounting for the camera FoV, accuracy requirements, and dimension constraints, a solution using two light-emitting diodes (LEDs) patterns has been designed and is depicted in Figure 6.

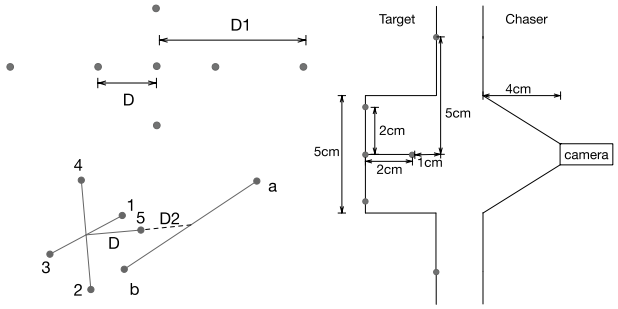

Figure 6: LED pattern (left) and disposition in the middle of the docking port (right).

The inner pattern (LEDs 1 to 5) are mounted in a crossed-shape configuration and the LEDs a and b along with the 5th LED of the inner pattern constitute the outer pattern. Recovering the LEDs position on the camera CCD allows for obtaining a complete 6 DoF solution describing the coupled position and attitude between the LEDs and the camera. The outer pattern is used from 10 m to 5 m range. As the 5th LED is only 1 cm away from the two outer LEDs a and b, the relative attitude is poorly observable and the target and chaser star trackers information are fused with the camera output in an EKF. From 5 m range, the navigation filter switches to the inner LED pattern. Because of the symmetric crossed-shape pattern, the 6DoF navigation solution can be directly obtained either using an EKF or using an analytical solution presented in [25]. At docking, this navigation solution has been shown to provide an accuracy better than 0.1 mm and 0.2 deg along each axis. A critical aspect is the sensitivity and robustness of the VBN to sun blinding, stray light and reflections on the CubeSat structure. The LEDs have a wavelength of 470 nm and the camera is equipped with a band-pass filter centred at this frequency which helps reducing stray light and other optical perturbations. To assess the robustness of the VBN, a lab experiment has been designed using a 6U CubeSat front panel, integrating the LEDs, and a sun simulator. This is shown in Figure 7 a). Different angles between the Sun simulator and the camera have been tested, of which the case where the sun is perpendicular to the camera, in its back and in its FoV. Using the geometrical properties of the LEDs pattern and the estimated 6 DoF solution (obtained either from the VBN or from the ADCS and CDGPS, together), reflections and stray light can be rejected as shown in Figure 7 b) and d). Note that due to the camera

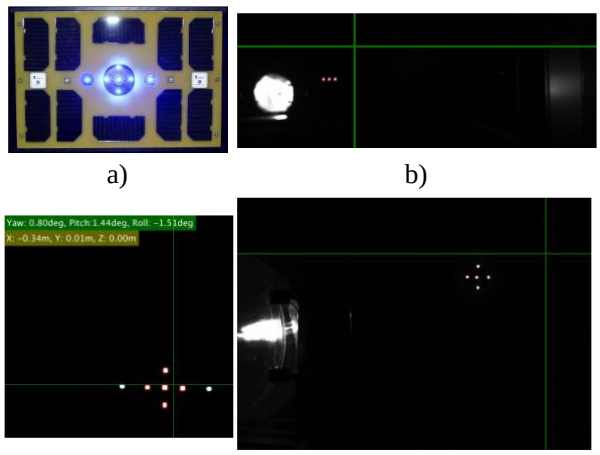

Figure 7: a) 6U surface mock-up, b) outer pattern detected at 10 m with the sun simulator, c) inner pattern detected and analytical solution, d) inner pattern detected at 1 m and sun simulator.

short exposure time (35 µs), the LEDs can be detected even if the sun is in the camera FoV. Finally, Figure 7 c) shows the full LED pattern at a range of 34 cm and the analytical solution is displayed. This VBN solution can thus be used in any illumination condition and is thus not a limiting factor for docking.

3.3 Control

The translation actuation is performed using an updated version of the GomSpace cold gas propulsion system [26]. It assumes four 1 mN thruster per axis. The minimum impulse time is 25 ms. It is operated in pulse width modulation (PWM) and an error of 5% on the pulse duration and 5% on the thrust level is considered. Furthermore, it is assumed that CoM errors will convert 5% of the thrust output into torque disturbance. The PWM effect on a command force input is shown in Figure 8.

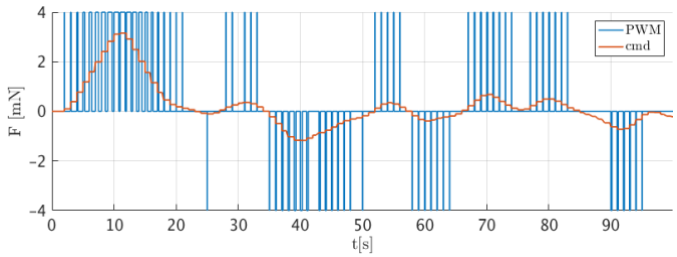

Figure 8: Propulsion output.

The gaps in the thrust profile are due to command forces that are smaller than the minimum impulse bit. For the closing, from 500 m to 10 m range, LQR and H∞ are traded-off, ensuring the closed-loop tracking during the Rbar manoeuvres. They all have been tuned considering the chaser dry mass, i.e. 10 kg. The LQR tuning requires the definition of two weights R and Q appearing in the cost function:

$$J = \int_0^\infty dt\,(\boldsymbol{x}^T Q \boldsymbol{x} + \boldsymbol{u}^T R \boldsymbol{u}) \qquad (1)$$

The controller is tuned using the usual initial guess for the Q and R matrices:

$$Q_{ii} = \frac{1}{{x_{max}}^2},\ R_{ii} = \frac{1}{{F_{max}}^2} \qquad (2)$$

where x_{max} is the allowed maximal error and F_{max} the maximum available control input.
An exhaustive theoretical description of H∞ synthesis can be found in [27]. The basic principle is depicted on Figure 9. The aim is to find a controller which minimizes the infinity norm of the transfer

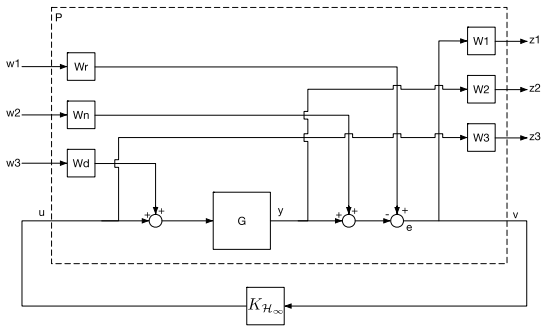

Figure 9: H_∞ problem.

function from the exogenous input w to the output z. If the infinity norm is smaller than one (i.e. 0 dB), no signal is amplified between w and z. Here, the inputs are the reference signal, sensor noise and external disturbances (environment and actuators). The outputs are the sensitivity function S, the complementary sensitivity function T, and the plant input sensitivity KS, where K is the controller. The weights W_r, W_n, and W_d are transfer functions describing the frequency content of the inputs. W_1, W_2, and W_3 are transfer functions used to shape S, T and KS.

Although very simple to tune, the LQR design does not have integral action. Thus, for the closing, from 500m range (S2) to 10 m range ($S2_4$), 3 different LQR are tuned according to the level of accuracy which increases along the approach. A low bandwidth (LB) controller is used from 500 m to 150 m. A medium bandwidth (MB) controller is used from 150 to 50 m, and finally a high bandwidth (HB) is used until 10 m (S3). Using H_∞, only two controllers are necessary. A LB is used from 500 m to 50 m and a HB for the remaining part of the closing. The reason is that in H_∞ design the sensitivity function of the LB controller can be decreased at low frequencies, using the weights W_1, thus increasing the integral action and reducing steady state errors.

For the P2P control, three controllers are under consideration and traded-off: LQR, H_∞ and μ-synthesis. The H_∞ and μ-synthesis design for the 6 DoF coupled control are described in [28]. The robust stability (RS) of a controller to a bounded set of uncertainties can be assessed using μ-analysis [29]. The chaser has a dry mass of 10 kg and can carry 2 kg of propellant. Its total mass can thus vary in the interval [10 kg, 12kg]. CubeSats inertia tensor are typically estimated using 3D modelling software and the accuracy is estimated to be 10%. The sloshing model used inside the dynamics is described in [30]. It is composed of two uncertain parameters. The damping coefficient has an uncertainty of 48% and 40% for the Eigen frequency. The effect of the RW and propulsion uncertainties has simply been modelled by a gain matrix at the plant input with 10% uncertainties for the torques and forces. Finally, all the different delays in the loop are accounted for in a single delay at the plant input. The GNC being sampled at 1Hz, the time delay is estimated to take values between zero and one second. μ-analysis shows that all the controllers are robustly stable to the set of bounded uncertainties and can tolerate up to ~190% of the modelled uncertainties. A crucial element that the μ-analysis provides is the sensitivity of the controllers to the different uncertainties. Here, the sloshing and input uncertainties are the dominant sources of instabilities. This information can then be used to design controllers less sensitive to these parameters, as it has been done for the μ-synthesis presented in [28], or to invest resources in the development of more accurate actuators or anti-slosh baffle in the propulsion tanks. Note that all the controllers have been designed using the MATLAB® robust control toolbox [31]. Finally, as the GNC is sampled at 1 Hz, the controllers have to be discretised. This is done using a bilinear transformation as it preserves the H_∞ norm [32].

4 DOCKING MECHANISM

The docking mechanism has been designed so that the following characteristics are respected:

- The mechanism is composed of two parts, one active mounted on the chaser and one passive mounted on the target.
- The volume occupation of each part is equal or less than 0.5U.
- A clearance of Ø50 mm minimum is reserved at the centre of the docking unit to allow for the VBN metrology system integration.

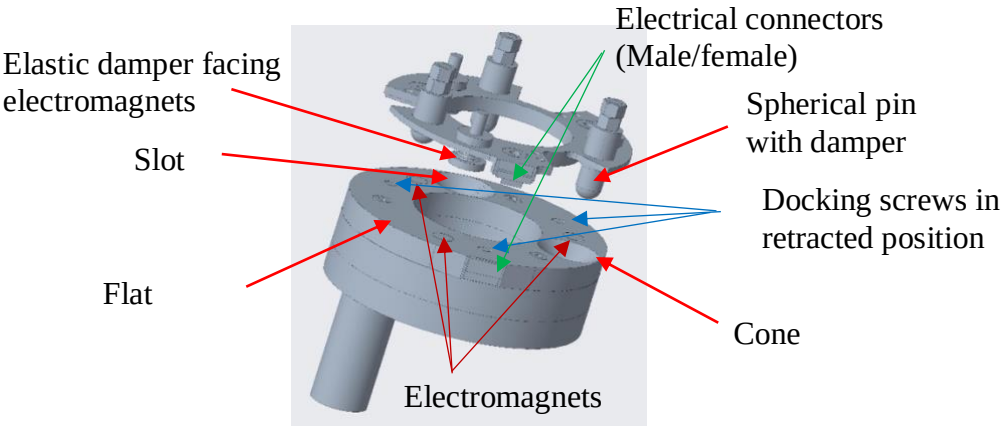

Figure 10: Complete docking mechanism.

Figure 10 shows the two parts of a prototype compliant with the above characteristics, except for the motor which has not been optimized at this level of development but can easily be replaced by a flat actuator. The mechanism is mounted on the test facility described in Figure 12. The mechanical docking process is achieved in three steps:

1. Approach and alignment controlled by the GNC as described above to reach the convergence of the two parts (active and passive) within an alignment accuracy of 1 cm and angular misalignment of 2 deg maximum.
2. Soft docking: three spherical pins situated on the passive part enter in contact with three corresponding areas. The 6 DoF of the mechanical alignment are fixed when the spheres reach a stable position at the apex of the cone, slot and flat seating (see Figure 10). Elastic dampers and switchable electromagnets, activated only during the docking phase, are designed to prevent re-bouncing of the parts.
3. Hard docking: once the alignment is stabilised, the active part of the mechanism actuates three screws synchronously that secure tightly the passive part. The electromagnets are switched off so that no further magnetic disturbances are generated and no more power is required.

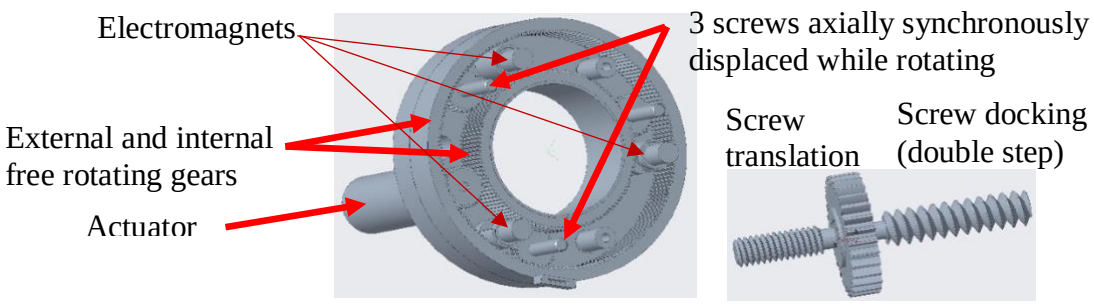

Figure 11: Docking screws mechanical synchronisation.

The docking with three coupled screws requires that the alignment with the opposite threaded bore hole is well aligned. This is achieved with the three points constraining device described in the soft docking explanation. It is furthermore necessary that the screws are engaged simultaneously in their respective tapped holes in order to prevent any jamming. The device presented in Figure 11 guarantees a synchronous rotation. The axial displacement of each screw is fully dependant on its

angular position. The docking screw step size is double that of the screw translation. When rotating, the screw first translates outwards the mechanism until the connection with the opposite tapped hole is reached. While the screw translation continues, the docking screws pulls back the passive part, compressing further the damping springs while penetrating further within it. Eventually an end stop is reached. The hard docking is completed. The accurate mechanical alignment and parallel displacement during the last docking step allow for an electrical connection mating to be achieved between the two docked parts.

4.1 Testing

A demonstrator based on this design has been manufactured and its functions have been tested in the laboratory. While the mechanical functions are easily tested in static conditions, that is when the passive and active parts are approached and aligned manually, the critical aspects of initial misalignment that would occur in orbit are much more difficult to handle on earth. The development of a testing facility could, although not fully but at least demonstrate that docking has been effectively achieved in dynamical conditions in presence of misalignment.

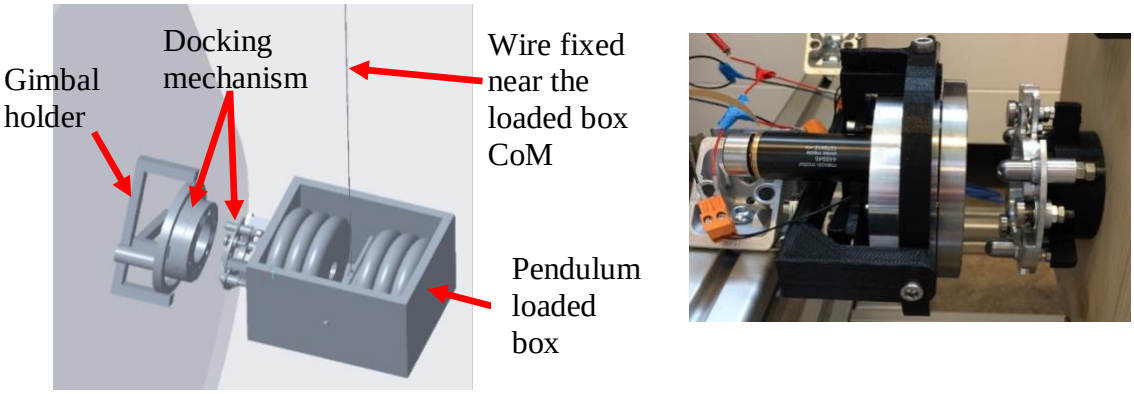

Figure 12: Test setup (left) and actual mechanism (right).

The pendulum wire length defines a controllable velocity at impact for a given deviation from stable position. The almost free angular movement of the box around the attachment point of the pendulum allows for unconstrained angular deviation with respect to the ideal mechanism alignment. Furthermore, the gimbal holder allows for defined angular tilt from one to two degrees. The pendulum allows to achieve a velocity of 2 cm/s at docking and the box has a mass of 20 kg. This is conservative compared to the current GNC and CubeSat design. The pendulum trajectory is not accurately controllable. The VBN solution described in section 3.2 placed on the pendulum has been used to measure the exact position at impact and correlate it with the occurrence or non-occurrence of docking. The observation of more than 100 impacts with various misalignment and tilt angles have shown more than 80% have ended by a successful docking. The failures could be explained either by too large misalignments when releasing the pendulum or by the testing conditions far from being ideal. Some improvements of the mechanism have also been proposed, in particular with respect to the damping functions. Their implementation in the coming developments will significantly enhance the docking likelihood. Overall, this simple experiment setup gives confidence that the mechanism can indeed handle 1 cm and 2 deg relative misalignment.

5 RESULTS

Before presenting the closing and docking results, the ADCS performances will be provided. The orbit is a 6AM Sun Synchronous Orbit with a 600 km altitude. Although the eclipse time are optimal on such orbit, the various sensors are manually activated/deactivated to simulate worst case

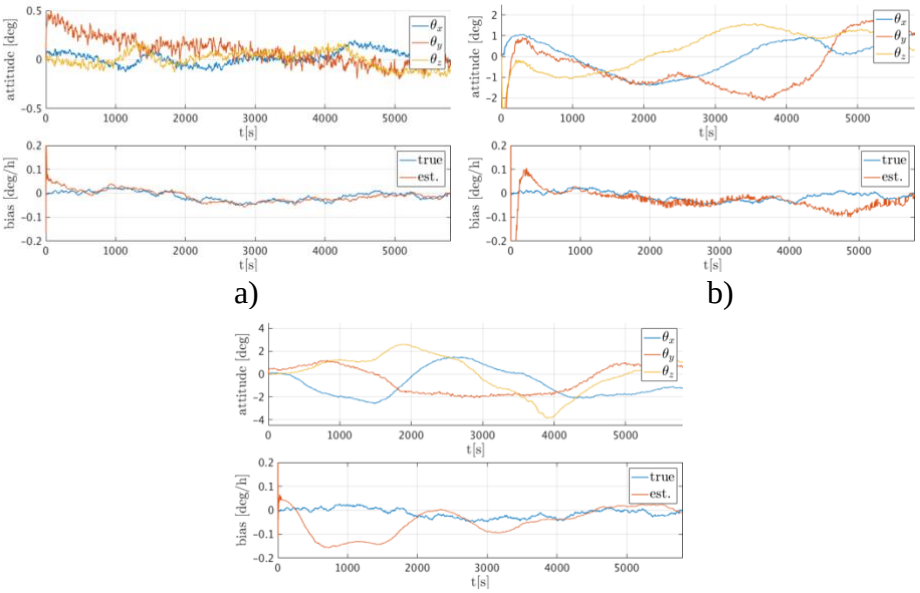

Figure 13: Pointing accuracy and bias with: a) the star tracker, magnetometer and gyroscope, b) the sun sensors, magnetometer and gyroscope, c) the magnetometer and gyroscope.

conditions, such as to be representative of a variety of orbits. The nominal scenario assumes that the star tracker, magnetometer and gyroscopes are available. The sun sensors are not used if the star tracker is available as their errors tend to decrease the ADCS performance. Even if the magnetometers are expected to be calibrated, a residual dynamic bias is assumed. As it is difficult to obtain actual data, a dynamic bias amounting 2% of the local Earth magnetic field is included in the simulations, which correspond to ~0.8μT. Three scenarios covering all possible situations are shown in Figure 13. For each scenario, the attitude error and bias estimation are provided. The nominal scenario assumes the star tracker, magnetometer, and gyroscope are available (Figure 13 a) and will be used for the docking simulations and has a maximum Absolute Performance Error (APE) of 0.5 deg. Note that, θ_y is less accurate than the other axis. The reason is that the star tracker is pointed towards the $+\hat{y}$ direction of the body frame and its noise is more important along its boresight. The two other scenarios represent a loss of star tracker when out of eclipse (Figure 13 b, max. APE=2.1 deg) and in eclipse (Figure 13 c, max. APE=3.8 deg). The importance of having a reliable gyros and bias estimation in the EKF for such a mission is critical as it allows to maintain a pointing accuracy using only the magnetometers and the gyros. Regardless of the attitude scenario, the closing and docking remains possible.

For the closing, the required accuracy is 5% of the range. A total of 250 Monte-Carlo simulations are required to have a confidence interval representing 10% of the requirement, i.e. 0.5% of the range, with a 95% confidence level. The uncertainties described in section 3.3 are used for the simulation

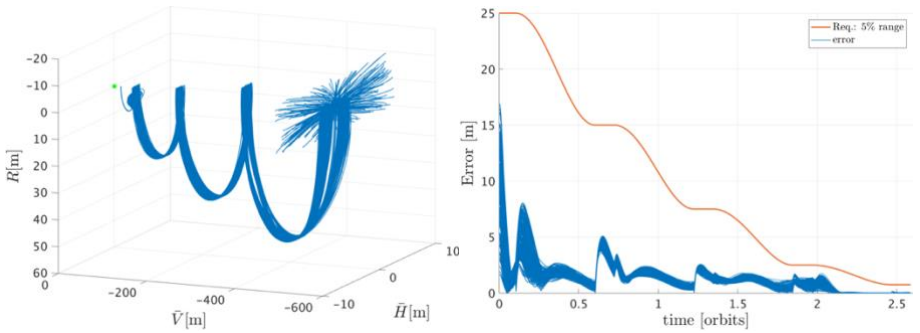

Figure 14: Closing, H∞: LVLH position (left), error (right), ΔV=0.67 m/s.

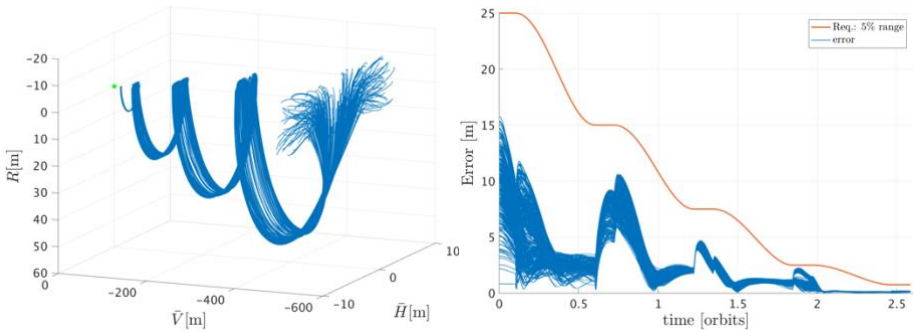

Figure 15: Closing, LQR: LVLH position (left), error (right), ΔV=0.51 m/s.

along with an initial position uncertainty. Furthermore, a 50% uncertainty on the VBN noise is assumed. The results are provided in Figure 14 for the H_∞ and in Figure 15 for the LQR. At each SK point along the closing, the chaser waits for 10 min before initiating the next manoeuvre. The total ΔV for the closing is 0.67 m/s for the H_∞ and 0.51 m/s for the LQR which means that, the closed-loop control consumes more than 61% of the total ΔV for the H_∞, and 49% for the LQR. The LQR consumes ~0.16 m/s less than the H_∞. However, its accuracy is worse than the H_∞ as the LQR does not have integral action. Furthermore, the H_∞ requires only two different controllers, as opposed to the LQR which requires three. Thus, from an implementation and safety perspective, the H_∞ seems more appropriate.

The last part of the RVD scenario, from point $S2_4$ to docking is shown in Figure 16 for the H_∞ and in Figure 17 for the LQR. Recall that the target docking port is rotated by 50 deg around each axis. In both case, the LVLH position is shown on the left of the figure and the trajectory in the docking frame is shown on the right. The red lines represent the 5% of the range accuracy requirement. At 10m range, the handover to the 3 LEDs VBN took place. The 3 LEDs EKF is initiated with the star trackers in the loop but they are not used afterwards for the translation and thus an ISL is not required as soon as the VBN filters have converged. At 5 m the handover between the 3 LEDs and 5 LEDs VBN occurs. The total time from 15 m until docking takes 1h 20min and requires 0.35 m/s of ΔV for the H_∞, and 0.23 m/s for the LQR. As for the closing, the LQR consumes less fuel but has more

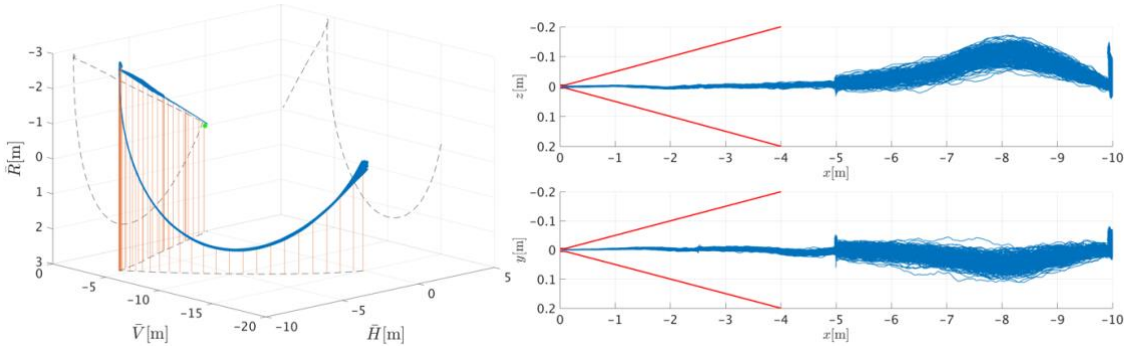

Figure 16: Docking, H_∞: LVLH position (left), P2P position (right), ΔV=0.35 m/s.

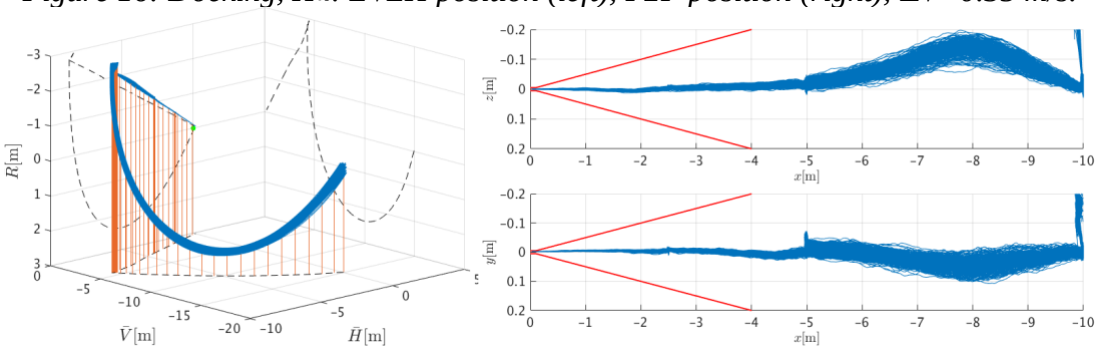

Figure 17: Docking, LQR: LVLH position (left), P2P position (right), ΔV=0.25 m/s.

dispersion. Consequently, the total ΔV for a RVD mission using H_∞ control is 1.02 m/s and 0.74 m/s for the LQR.

To increase the confidence for the docking, 600 simulations have been performed from 5m range until docking. This leads to a confidence interval of 0.3 mm on the 5 mm requirement with 95% confidence. Figure 18 shows the docking accuracy and the relative attitude for three controllers: LQR, H_∞, and μ-synthesis. Note that the μ-synthesis controller has the same structure than the H_∞ but is made more robust to input gain and sloshing uncertainties. The three controllers are well within the requirement and would thus lead to a successful docking. It should be noted that although the LQR seems to perform better, it has actually a larger systematic bias due to its lack of integral action. This fact is even more important for a scenario where the target docking port would be aligned with the V-bar axis of the LVLH frame. This is shown in Figure 19 and it can be seen that the LQR barely satisfies the requirement as opposed to the other controllers which have very similar performances for both scenarios. The large LQR bias could be removed by adding a pre-compensator which could partially replace the integral action that the H_∞, and μ-synthesis have. However, as opposed to integral action, the pre-compensator will have to be retuned manually for each docking port orientation.

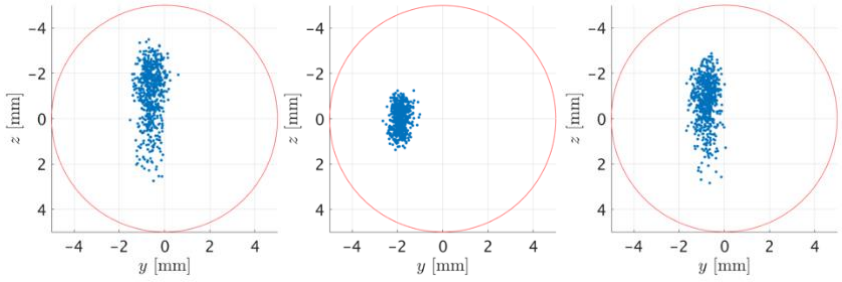

a) b) c)

Figure 18: Relative position and attitude accuracy at docking: a) H_∞, b) LQR, and, c) μ-synthesis.

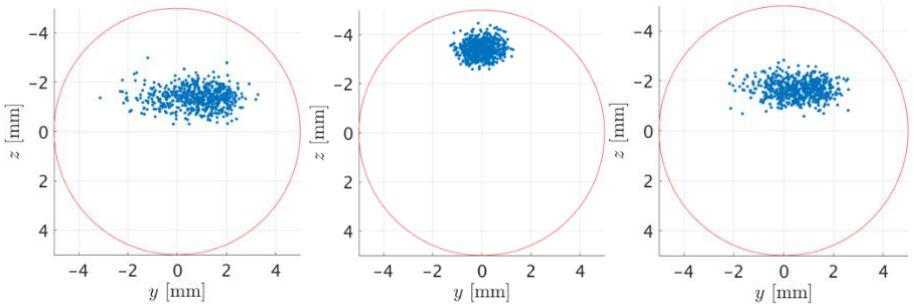

a) b) c)

Figure 19: Relative position docking for a V-bar aligned scenario: a) H_∞, b) LQR, and, c) μ-synthesis.

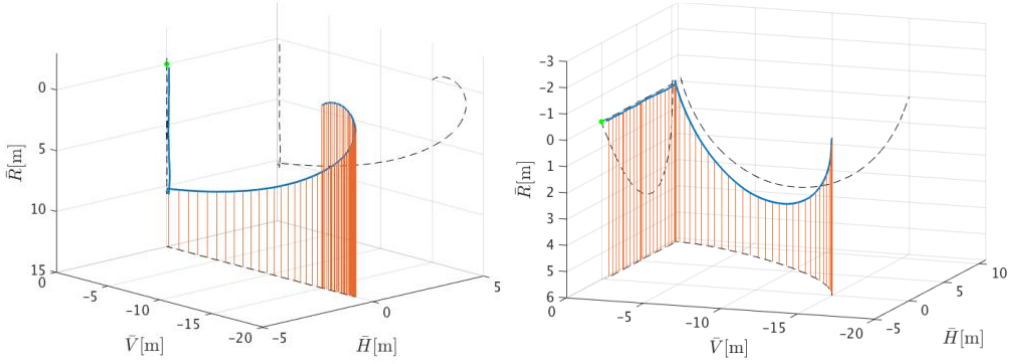

Figure 20: R-bar docking (left) and H-bar docking (right).

Finally, two extra docking scenarios are provided in Figure 20. It shows a docking along R-bar and H-bar. In both case the docking requirements have been satisfied. Thus, docking along any direction in the LVLH frame can be successfully achieved.

6 CONCLUSION

In this paper, a dedicated GNC for CubeSat RVD has been proposed. A VBN system allows for 6 DoF relative navigation from 10 m range. It has been designed to be incorporate in a dedicated docking mechanism. The mechanism and VBN fit in 0.5U and can thus be used on a variety of CubeSats. Three different controllers have been traded-off and all lead to successful closing and docking. The controllers combined with the various navigation techniques provide a position accuracy better than 5% of the range and a docking accuracy better than 5 mm, with margins. Based on these results, it is hard to give the preference to a control scheme in particular. However, because the LQR does not have integral action, it has exhibited more bias than the H_∞ or the μ-synthesis. A pre-compensator could be included but it would need to be specifically tuned for each mission, which is a clear disadvantage. However, the LQR consumes on average 25% less fuel. The design of an H_∞ or μ-synthesis controller requires the tuning of several weighting function. The large number of parameters makes the fuel optimisation by hand complicated although more optimal controllers could certainly be obtained. This shall be further studied. Several docking scenarios have been simulated and it shows that the proposed GNC can handle a variety of docking configurations without need for retuning the controllers or the navigation. This is a considerable advantage as this will allow to cope with any situations in orbit.
The results of 600 Monte Carlo simulations have provided a confidence interval of 0.3 mm on the 5 mm (3σ) docking requirement with a 95% confidence. The simulations including realistic environment, sensors and actuators models, it is concluded that the docking of two CubeSats is feasible today using existing technologies, thus paving the way for the implementation of in-orbit demonstrators such as planned in the ESA RACE mission.

7 AKNOWLEDGEMENTS

This work was supported by the European Space Agency Networking/Partnering Initiative (NPI) programme (contract No. 4000112462/14/NL/GLC). The authors would like to thank the students who helped in the design of the docking mechanism: Mr Dimitri Goutaudier, Mr Félix Martel, Mr Alberto Rigamonti, and Mr Malik Fahrni.

8 REFERENCES

[1] S. Nolet, E. Kong, and D. W. Miller, 'Autonomous docking algorithm development and experimentation using the SPHERES testbed', in *Proceedings of SPIE*, 2004, vol. 5419, pp. 1–15.
[2] C. Pirat *et al.*, 'Mission design and GNC for In-Orbit Demonstration of Active Debris Removal technologies with CubeSats', *Acta Astronautica*, vol. 130, pp. 114–127, Jan. 2017.
[3] L. Olivieri and A. Francesconi, 'Design and test of a semiandrogynous docking mechanism for small satellites', *Acta Astronautica*, vol. 122, pp. 219–230, May 2016.
[4] L. Rodgers, N. Hoff, E. Jordan, M. Heiman, and D. W. Miller, 'A Universal Interface for Modular Spacecraft', in *Proceedings of the 19th Annual AIAA/USU Conference on Small Satellites*, Logan, Utah, 2005.
[5] S. D'Amico, J.-S. Ardaens, and S. De Florio, 'Autonomous formation flying based on GPS — PRISMA flight results', *Acta Astronautica*, vol. 82, no. 1, pp. 69–79, Jan. 2013.
[6] W. Fehse, *Automated rendezvous and docking of spacecraft*, vol. 16. Cambridge university press,

2005.
[7] D. Pinard, S. Reynaud, P. Delpy, and S. E. Strandmoe, 'Accurate and autonomous navigation for the ATV', *Aerospace Science and Technology*, vol. 11, no. 6, pp. 490–498, Sep. 2007.
[8] G. Casonato and G. B. Palmerini, 'Visual techniques applied to the ATV/1SS rendezvous monitoring', in *Aerospace Conference, 2004. Proceedings. 2004 IEEE*, 2004, vol. 1.
[9] B. E. Tweddle and A. Saenz-Otero, 'Relative Computer Vision-Based Navigation for Small Inspection Spacecraft', *Journal of Guidance, Control, and Dynamics*, vol. 38, no. 5, pp. 969–978, 2015.
[10] 'DLR - Space Operations and Astronaut Training - Phoenix Miniature GPS Receiver'. [Online]. Available: http://www.dlr.de/rb/en/desktopdefault.aspx/tabid-10749/10533_read-23353/. [Accessed: 19-Mar-2018].
[11] 'ZARM Technik: Magnetometer'. [Online]. Available: http://www.zarm-technik.de/products/magnetometer/. [Accessed: 19-Mar-2018].
[12] N. A. Matteo and Y. T. Morton, 'Ionosphere geomagnetic field: Comparison of IGRF model prediction and satellite measurements 1991-2010: VALIDATION OF IGRF', *Radio Science*, vol. 46, no. 4, p. n/a-n/a, Aug. 2011.
[13] 'ST200', *Hyperion Technologies B.V.* [Online]. Available: http://hyperiontechnologies.nl/products/st200-star-tracker/. [Accessed: 23-Jun-2017].
[14] 'Sensonor - STIM300', *sensonor.no*. [Online]. Available: https://www.sensonor.com/products/inertial-measurement-units/stim300/. [Accessed: 19-Mar-2018].
[15] J. Vandersteen, R. Walker, and J. Vennekens, 'Nano- to small satellite pointing errors: limits of performance', ESA, ESTEC, Oct. 2015.
[16] 'IEEE Standard Specification Format Guide and Test Procedure for Single-Axis Laser Gyros', *IEEE Std 647-1995*, pp. 1–88, May 1996.
[17] J. Vandersteen, 'Reaction wheels: Friction and instabilities', ESA, ESTEC, May-2014.
[18] 'CubeWheel Large - CubeSatShop.com'. [Online]. Available: https://www.cubesatshop.com/product/cubewheel-large/. [Accessed: 19-Mar-2018].
[19] 'RW400', *Hyperion Technologies B.V.* [Online]. Available: http://hyperiontechnologies.nl/products/rw400-series-reaction-wheel/. [Accessed: 19-Mar-2018].
[20] J. Vandersteen, 'Modelling of reaction wheel cage instabilities', ESA, ESTEC, Jan. 2013.
[21] F. L. Markley and J. L. Crassidis, *Fundamentals of Spacecraft Attitude Determination and Control*. New York, NY: Springer New York, 2014.
[22] 'MTQ400', *Hyperion Technologies B.V.* [Online]. Available: http://hyperiontechnologies.nl/products/mtq400/. [Accessed: 19-Mar-2018].
[23] J. MURRELL, 'Precision attitude determination for multimission spacecraft', in *Guidance and Control Conference*, American Institute of Aeronautics and Astronautics, 1978.
[24] B. Wie, H. Weiss, and A. Arapostathis, 'Quarternion feedback regulator for spacecraft eigenaxis rotations', *Journal of Guidance, Control, and Dynamics*, vol. 12, no. 3, pp. 375–380, May 1989.
[25] C. Pirat, F. Ankersen, R. Walker, and V. Gass, 'Vision Based Navigation for Autonomous Cooperative Docking of CubeSats', *Acta Astronautica*, vol. 146, pp. 418–434, May 2018.
[26] 'GOMspace | NanoProp 6U propulsion'. [Online]. Available: https://gomspace.com/Shop/subsystems/propulsion/nanoprop-6u-propulsion.aspx. [Accessed: 24-Mar-2018].
[27] S. Skogestad and I. Postlethwaite, *Multivariable Feedback Control: Analysis and Design, 2nd Edition*. Wiley New York, 2005.
[28] C. Pirat, F. Ankersen, R. Walker, and V. Gass, 'H∞ and μ-Synthesis for Nano-Satellites Rendezvous and Docking', Submitted for publication 2018.
[29] J. Doyle, 'Analysis of feedback systems with structured uncertainties', in *IEE Proceedings D-Control Theory and Applications*, 1982, vol. 129, pp. 242–250.
[30] F. Ankersen, 'Guidance, Navigation, Control and Relative Dynamics for Spacecraft Proximity Maneuvers', Aalborg University, Aalborg, 2011.
[31] G. Balas, R. Chiang, A. Packard, and M. Safonov, 'Robust control toolbox R2017b', *The MathWorks, Inc., Natick, Massachusetts, United States*, 2017.
[32] M. Green and D. J. Limebeer, *Linear robust control*. Courier Corporation, 2012.